

Janus Metastructure Based on Magnetized Plasma Material with and Logic Gate and Multiple Physical Quantity Detection

Junyang Sui, Ruiyang Dong, Siyuan Liao, Zeyuan Zhao, Yubo Wang, and Hai-Feng Zhang*

In this paper, a Janus metastructure (JMS) is proposed that can act both as a logic gate and detect multiple physical quantities. By adjusting the incident angle of electromagnetic waves, arranging the dielectrics asymmetrically, and using the anisotropy of the plasma, the Janus function can be obtained, which gives the metastructure a multiscale property. Sharp transmission peak (TP) is generated by located defect mode resonance. The AND logic gate on the positive and negative scales can be realized by judging the TP value. By locking the point frequency of the TP, the refractive index, magnetic field strength, incident angle, and plasma density can be detected simultaneously on the two scales in the GHz range, which is rarely studied. Good sensing performances are also owned, and the corresponding optimal sensitivities are $0.095 (2\pi c/d)/RIU$, $9.42 \times 10^{-3} (2\pi c/d)/T$, $1.48 \times 10^{-3} (2\pi c/d)/^\circ$, and $0.035 (2\pi c/d) m^3/10^{19}$, respectively. Compared with the traditional sensors, the proposed JMS equipped with two scales not only can realize the logic gate but also measure multiple physical quantities, which has a certain application potential.

has been extended to quasiperiodic structures formed by artificially packed mediums, known as metastructure (MS), by breaking the symmetry of the structure to gain controllability over the different electromagnetic waves (EWs) propagation directions. The Janus metastructure (JMS) with different positive and negative transmissivity (T) has achieved dynamic holograms in the visible and microwave regions.^[9,10] In addition, JMSs have physical properties and functions not found in natural structures, such as black holes,^[11] wave absorption,^[12–15] and stealth.^[16–18] Furthermore, since it can control the propagation mode of EWs, including amplitude and phase,^[19,20] polarization,^[21,22] and angular momentum,^[23] the JMS is widely used in the manufacture of logic gates,^[24] isolators,^[25] and filters.^[26]

In recent years, optical logic gate devices have attracted wide attention due

1. Introduction


Janus is the god of beginnings in Roman mythology. He has two faces, looking to the past and the future.^[1] Inspired by this implication, scientists have named two-sided particles Janus particles,^[2–4] which possess different materials on opposite sides. The anisotropy and directionality of the materials give Janus particles inconsistent forward and backward functions and additional controllability.^[5–8] More recently, a similar Janus function

to their important applications in optical computing and ultrahigh-speed information processing, such as photonic microprocessors,^[27,28] optical signal processors,^[29–32] and all-optical processors.^[33] Due to the features that the photonic bandgap (PBG) of the JMS can control the propagation of EWs, the optical logic gate can be realized by constructing multimode interference waveguides to adjust the PBG of the JMS and the phase of the input EWs.^[34] Therefore, the JMS is the best candidate material to achieve the optical logic function.^[35] Logic gates based on JMS have the properties of compact structure, fast speed, and low power consumption.

With the rapid development of sensor research, it has become the focus of discussion among researchers. Together with computer technology and information exchange technology, it has become the three key technologies in the information industry.^[36] Optical sensors are considered a promising tool for physical quantity detection due to their high sensitivity (S), no label, and real-time monitoring. On account of the good demodulation feature of the Mach–Zehnder interferometer and the excellent resonance property of the liquid-crystal infiltrated photonic crystals (PC) cavity, Zhao et al.^[37] presented a miniaturized high S electric field sensor based on the PC cavity, whose S and detection limit (DL) are $7 \text{ nW per V m}^{-1}$ and 0.143 V m^{-1} , respectively.

J. Sui, S. Liao, H.-F. Zhang
College of Electronic and Optical Engineering & College of Flexible Electronics (Future Technology)
Nanjing University of Posts and Telecommunications (NJUPT)
Nanjing 210023, P. R. China
E-mail: hanlor@njupt.edu.cn

R. Dong, Z. Zhao, Y. Wang
Bell Honors School
Nanjing University of Posts and Telecommunications (NJUPT)
Nanjing 210023, P. R. China

 The ORCID identification number(s) for the author(s) of this article can be found under <https://doi.org/10.1002/andp.202200509>

DOI: 10.1002/andp.202200509

Table 1. The performance of the JMS on the positive and negative scales.

Physical quantity	Parameter	Positive scale	Negative scale
RI	Detection range	$\approx 2\text{--}2.75$	$\approx 1.9\text{--}3.5$
	S	$0.095 \alpha \text{ RIU}^{-1}$	$0.086 \alpha \text{ RIU}^{-1}$
B_1	Detection range	$\approx 2\text{--}2.15 \text{ T}$	$\approx 1.96\text{--}2.16 \text{ T}$
	S	$9.42 \times 10^{-3} \alpha \text{ T}^{-1}$	$4.47 \times 10^{-3} \alpha \text{ T}^{-1}$
B_2	Detection range	$\approx 1.55\text{--}1.65 \text{ T}$	$\approx 1.51\text{--}1.71 \text{ T}$
	S	$2.57 \times 10^{-3} \alpha \text{ T}^{-1}$	$7.88 \times 10^{-3} \alpha \text{ T}^{-1}$
θ	Detection range	$\approx 15^\circ\text{--}35^\circ$	$\approx 22^\circ\text{--}52^\circ$
	S	$1.08 \times 10^{-3} \alpha \text{ degree}^{-1}$	$1.48 \times 10^{-3} \alpha \text{ degree}^{-1}$
n_e	Detection range	$\approx 0.75\text{--}1.1 (10^{19} \text{ m}^{-3})$	$\approx 0.58\text{--}1.13 (10^{19} \text{ m}^{-3})$
	S	$0.035 \alpha \text{ m}^3 10^{-19}$	$0.034 \alpha \text{ m}^3 10^{-19}$

Yang et al.^[38] designed a temperature-insensitive hydrogen sensor on the strength of the polarization-maintained PC fiber, with $S = 131 \text{ pm}\%$ in the range of $\approx 1\text{--}4 \%$ hydrogen concentration. Sovizi et al.^[39] proposed to use the defect mode of 1D MS based on the layers of silicon, analyte, and silica as the refractive index (RI) sensor, and the S belonging to vertical and 45 incident angle was severally greater than 450 and 600 nm RIU^{-1} . The above reports can realize the detection of physical quantities and possess good sensing performance at the same time, but it exists a pity that the realized function is single. Liu et al.^[40] designed a multiphysical quantity sensor based on D-type high-birefringence PC fiber surface plasmonic resonance effect, which could achieve ultrahigh S temperature and RI detection, and the corresponding maximum detection range and S were $\approx 36\text{--}86 \text{ }^\circ\text{C}$, $-16.875 \text{ nm }^\circ\text{C}^{-1}$ and $\approx 1.43\text{--}1.5$, $44850 \text{ nm RIU}^{-1}$, respectively. The multifunctional sensor provides a new idea for relative field research, which has a certain research value.

In this paper, a 1D JMS based on magnetized plasma material is designed, which can realize the multifunction of the logic gate and multiphysical quantities detection on the positive and negative scales. After adjusting the incident angle of EWs and the asymmetrical arrangement of different dielectrics, the Janus function is implemented, which gives the MS the multiscale property **Table 1** (the performance of the JMS is shown in). The plasma is introduced into the structure as a defect layer to form a localized defect mode resonance (LDMR), resulting in a sharp transmission peak (TP). The plasma layer is affected by the magnetic field, which gives the device the ability of magnetic field tuning. By tuning the magnetic field strength (MFS), the TP can be utilized to realize the AND logic operation function on the positive and negative scales. The study of the proposed JMS also indicates that the resonant frequency corresponding to the TP will change when the physical quantities of the structure change. The RI, MFS, angle, and plasma density can be sensed by locking the TP frequency, which is rarely studied. It is worth mentioning that while carrying out multi-physical quantities detection, the AND logic operation is also strictly followed, which is the highlight of this paper. Such a JMS with multiscale, multifunction of logic operation, and multiphysical quantities detection can meet the application requirements in a variety of scenarios, which has certain research value and prospects (See **Table 2**).

Table 2. The AND logic gate truth table (the corresponding input and output states are in parentheses).

In_1	In_2	Ou
1 (B_1 exists)	1 (B_2 exists)	1 ($T > 0.9$)
1 (B_1 exists)	0 (B_2 does not exist)	0 ($T < 0.1$)
0 (B_1 does not exist)	1 (B_2 exists)	0 ($T < 0.1$)
0 (B_1 does not exist)	0 (B_2 does not exist)	0 ($T < 0.1$)

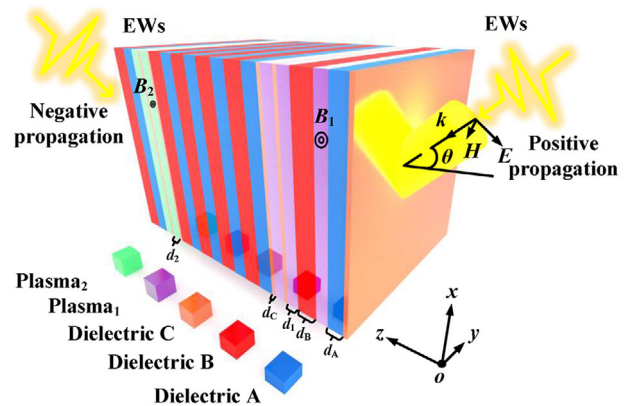


Figure 1. The proposed JMS consists of an asymmetric arrangement of dielectrics and plasma filled with different colors. Considering the universality of the results, d is selected as the normalized thickness, and $d = 140 \text{ nm}$. The thicknesses of the dielectric and plasma layers are $d_A = 0.1d$, $d_B = 0.3d$, $d_C = 0.0001d$, $d_1 = 0.012d$, and $d_2 = 0.016d$, respectively.

2. Design and Discussion

2.1. The Theoretical Model

The JMS in **Figure 1** can be fabricated by the etching method.^[41] The RI of dielectrics A, B, and C are $n_A = 2$, $n_B = 2.3$, and $n_C = 1$, severally. It should be emphasized that Leiwin et al. derived effective permittivity and permeability expressions for composites based on Mie resonance theory, and the desired RI can be obtained in a wide range.^[42] This technology has been applied in practice,^[43] so the permittivity set in this paper is reasonable and can be obtained in reality. The EWs are incident at an angle $\theta = 30^\circ$ from the positive and negative directions along the z -axis. MFS B_1 and B_2 paralleled to the y -axis are separately applied to layers of plasma₁ and plasma₂, and the initial values are set as $B_1 = 2 \text{ T}$ and $B_2 = 1.6 \text{ T}$. Since ordinary dielectrics are not affected by the magnetic fields, the coverage area of external magnetic fields is allowed to be larger than the thicknesses of the corresponding plasma layers in practical conditions. Moreover, since the areas where the layers of plasma₁ and plasma₂ locate in the JMS are far away from each other, the applied B_1 and B_2 do not interfere with each other. Considering the experimental application, Xuan et al. designed a gradient magnetic field coil. By applying current to it, a spatial linear magnetic field can be generated, which meets the requirements that the MFS on different plasma layers are precise and different.^[44] When EWs propagate in the 1D JMS, the EWs under TM polarization are affected by Lorentz's force. Nevertheless, under TE polarization, the propagating EWs in the structure are unacted on the magnetic fields B_1 and B_2 . The results show

that the 1D JMS based on plasma under magnetization has the same properties as the one under unmagnetization,^[45] so the situation under TM polarization is mainly considered. Depending on the normalized thicknesses of the mediums, the angular frequency at which EWs propagate can be normalized to $\omega = 2c\pi/d$, denoted by α .

The plasma dielectric function under TM polarization exhibits anisotropy, which can be expressed as follows^[46]

$$\epsilon_{\text{plasma}} = \begin{pmatrix} \epsilon_1 & 0 & i\epsilon_2 \\ 0 & \epsilon_3 & 0 \\ -i\epsilon_2 & 0 & \epsilon_1 \end{pmatrix} \quad (1)$$

Each of the tensors is^[46]

$$\epsilon_1 = 1 - \frac{\omega_p^2(\omega + iv_c)}{\omega[(\omega + iv_c)^2 - \omega_c^2]} \quad (2a)$$

$$\epsilon_2 = -\frac{i\omega_p^2\omega_c}{\omega[(\omega + iv_c)^2 - \omega_c^2]} \quad (2b)$$

$$\epsilon_3 = 1 - \frac{\omega_p^2}{\omega(\omega + iv_c)} \quad (2c)$$

where, ω_p , ω_c , v_c , and ω are plasma frequency, electron cyclotron frequency, plasma collision frequency, and normalized angular frequency of incident EWs, respectively. $\omega_p = (e^2 n_e / \epsilon_0 / m)^{1/2}$, $\omega_c = eB/m$, $v_c = 0.001\omega_p \cdot n_e = 1.1 \times 10^{19} \text{ m}^{-3}$, $e = 1.6 \times 10^{-19} \text{ C}$, $m = 9.1 \times 10^{-31} \text{ Kg}$, $\epsilon_0 = 8.8542 \times 10^{-12} \text{ F m}^{-1}$ severally represent plasma density, electron charge, electron mass, and dielectric constant in a vacuum. B is the strength of the magnetic field. The relative permittivity of the plasma under TM polarization is written as^[46]

$$\epsilon_{\text{TM}} = \frac{\epsilon_1^2 - \epsilon_2^2}{\epsilon_1} \quad (3)$$

So, the RI n_k ($k = 1$ or 2) of plasma₁ and plasma₂ can be obtained from $(\epsilon_k)^{1/2}$. For ordinary dielectric, the transfer matrix is given as^[47]

$$\mathbf{M}_j = \begin{pmatrix} \cos(k_{jz}d_j) & -\frac{i}{\eta_j} \sin(k_{jz}d_j) \\ -i\eta_j \sin(k_{jz}d_j) & \cos(k_{jz}d_j) \end{pmatrix} \quad (4)$$

where, j donated by A, B, and C symbolizes the corresponding dielectric. Under the TM polarization, the wave vector and optical admittance along the z -axis are represented by $k_{jz} = n_j\omega/c/\cos\theta_j$ and $\eta_j = (\epsilon_0/\mu_0)^{1/2}n_j/\cos\theta_j$. c and μ_0 are the speed of light and the permeability in a vacuum with values of $3 \times 10^8 \text{ m s}^{-1}$ and $4\pi \times 10^{-7} \text{ N m}^{-1}$. The transfer matrix belonging to the plasma layer is shown as^[47]

$$\mathbf{M}_k = \begin{pmatrix} \cos(k_{kz}d_k) + \frac{k_{kx}\epsilon_{xz}}{k_{kz}\epsilon_x} \sin(k_{kz}d_k) & -\frac{i}{\eta_k} \left[1 + \left(\frac{k_{kx}\epsilon_{xz}}{k_{kz}\epsilon_x} \right)^2 \right] \sin(k_{kz}d_k) \\ -i\eta_k \sin(k_{kz}d_k) & \cos(k_{kz}d_k) - \frac{k_{kx}\epsilon_{xz}}{k_{kz}\epsilon_x} \sin(k_{kz}d_k) \end{pmatrix} \quad (5)$$

where $k = 1$ or 2 indicates plasma₁ and plasma₂. The components of the wave vector on the x -axis and z -axis are $k_{kx} = \omega/cn_k \sin\theta_k$ and $k_{kz} = \omega/cn_k \cos\theta_k$, severally.

The entire transfer matrix \mathbf{M}_p on the positive scale is

$$\mathbf{M}_p = [\mathbf{M}_C \mathbf{M}_A \mathbf{M}_1 \mathbf{M}_B (\mathbf{M}_1 \mathbf{M}_C)^2 (\mathbf{M}_A \mathbf{M}_B)^4 (\mathbf{M}_C \mathbf{M}_2)^2 \mathbf{M}_A \mathbf{M}_B] \\ = \begin{pmatrix} m_{11} & m_{12} \\ m_{21} & m_{22} \end{pmatrix} \quad (6)$$

Similarly, when EWs propagate negatively, the entire transfer matrix \mathbf{M}_n is gained as

$$\mathbf{M}_n = [\mathbf{M}_B \mathbf{M}_A (\mathbf{M}_2 \mathbf{M}_C)^2 (\mathbf{M}_B \mathbf{M}_A)^4 (\mathbf{M}_C \mathbf{M}_1)^2 \mathbf{M}_B \mathbf{M}_1 \mathbf{M}_A \mathbf{M}_C] \\ = \begin{pmatrix} m_{11} & m_{12} \\ m_{21} & m_{22} \end{pmatrix} \quad (7)$$

Therefore, the reflection and transmission coefficients can be obtained^[46]

$$r = \frac{(m_{11} + m_{12}\eta_{N+1})\eta_0 - (m_{11} + m_{12}\eta_{N+1})}{(m_{11} + m_{12}\eta_{N+1})\eta_0 + (m_{11} + m_{12}\eta_{N+1})} \quad (8)$$

$$t = \frac{2\eta_0}{(m_{11} + m_{12}\eta_{N+1})\eta_0 + (m_{11} + m_{12}\eta_{N+1})} \quad (9)$$

in which, $\eta_0 = (\epsilon_0/\mu_0)^{1/2}/\cos\theta$. Since the backgrounds on both sides of the JMS are the same, $\eta_{N+1} = \eta_0$. The relevant reflectivity and T is^[46]

$$R = |r|^2 \quad (10)$$

$$T = |t|^2 \quad (11)$$

2.2. Analysis and Discussion of Performances

The functions achieved by the designed JMS are analyzed more clearly below. **Figure 2** shows the TP used for logic operation and physical quantities detection under magnetic control. The initial values of MSF B_1 and B_2 are set as 2 and 1.6 T and make B_1 and B_2 the first input "In₁" and the second input "In₂" respectively. When B_1 exists ($B_1 = 2$ T), the input level is "1," that is, "In₁ = 1," otherwise, the input level is "0." Similarly, "In₂ = 1" and "In₂ = 0" correspond to the input levels in the presence and absence of B_2 . "Ou" is used to represent the output. Judging the TP value generated under different conditions of B_1 and B_2 , if $T > 0.9$, the output level is "1," and "Ou = 0" symbolizes the output level when $T < 0.1$. Table 1 shows the truth table under the AND logic operation. The transmission spectra of EWs when propagating positively and negatively are severally indicated in Figure 2a,b. Since the 1D MS is tuned by MFS, the transmission spectra are significantly different under diverse applied MFS. When both B_1 and B_2 exist, that is, "In₁ = 1" and "In₂ = 1," sharp TPs are generated on the positive and negative scales, and the corresponding T is 0.902 and 0.92, which is greater than 0.9. At this moment, the output level is "Ou = 1," which satisfies the AND logic operation "1 AND 1 = 1." When only one magnetic induction density B_1 and B_2 exists or neither exists, as displayed in Figure 2a,b, the

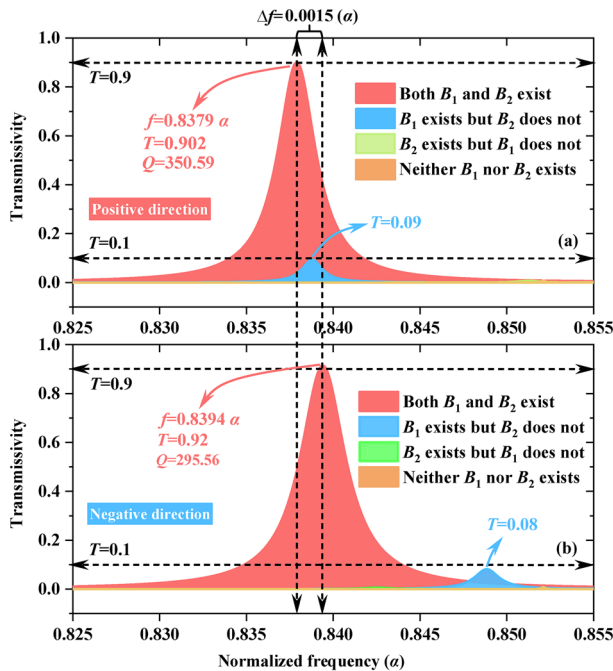


Figure 2. The transmission spectra formed under the modulation of magnetic fields B_1 and B_2 , realizing the AND logic function. a) When EWs are incident from the positive direction, and b) when EWs are incident from the negative direction.

values of TPs are less than 0.1, representing the output level of “Ou = 0,” which strictly follows the AND logic operation of “1 AND 0 = 0,” “0 AND 1 = 0,” and “0 and 0 = 0.” When “1 AND 1 = 1,” the quality factor (Q) of TP on the positive scale is 350.59, and the negative one is 295.56. $f = 0.8379 \alpha$ and $f = 0.8394 \alpha$ are frequency points belonging to the TPs, the frequency difference is $\Delta f = 0.0015 \alpha$, under the condition of $d = 140 \text{ mm}$, $\Delta f = 3.21 \times 10^6 \text{ Hz}$, easy to distinguish, which is the embodiment of the Janus property of the MS. This also means that the two scales can achieve the AND logical operation with the TPs owning different frequency points, T and Q . In addition, using the sharp TP generated by “1 AND 1 = 1,” the JMS can be taken advantage to detect weak fluctuations in RI, MFS, angle and plasma density.

To explain the cause of sharp TP, when the plasma layers of the JMS are absent, **Figure 3a** exhibits the value curves of reflectivity and T between normalized frequencies 0.825α and 0.855α in the case of positive incidence of EWs and the presence of both B_1 and B_2 . Obviously, the T is less than 0.1 in this range, and the reflectivity is greater than 0.9. PBG is obviously formed, and EWs are forbidden to propagate in the JMS. When the plasma layers are introduced into the structure as defect layers, the bandgap is adjusted, as indicated in **Figure 3b**, and a passband with T up to 0.902 is formed at $f = 0.8379 \alpha$. To observe the propagation of EWs in the structure more directly, and explain the reason why TP is generated. **Figure 4** shows the electric field energy distribution under the same case as **Figure 3b**. When the EWs propagate at 0.8379α ($f = 1.7955 \text{ GHz}$ when $d = 140 \text{ mm}$), at the surface of the plasma layer, the electric field is obviously localized and enhanced, which excites the LDMR, resulting in a sharp TP.

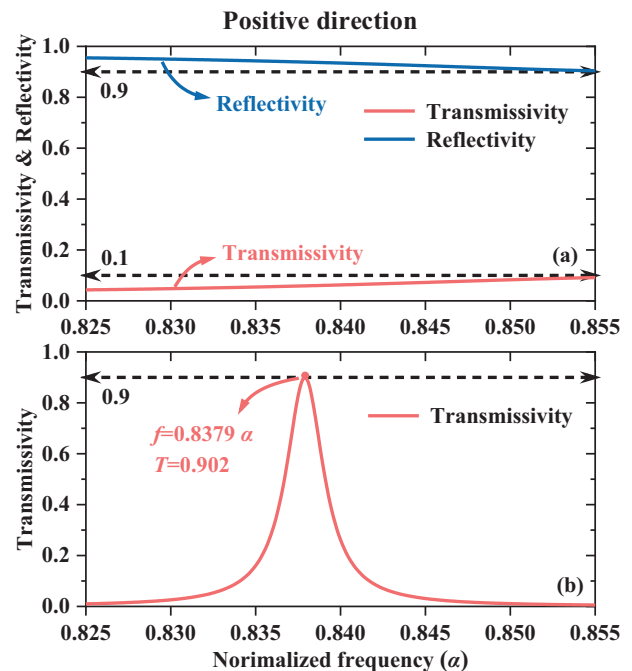


Figure 3. The diagram when EWs propagate positively under the presence of both B_1 and B_2 . a) The value curves of reflectivity and T under the absence of plasma layers, and b) The value curve of T under the introduction of plasma defect layers.

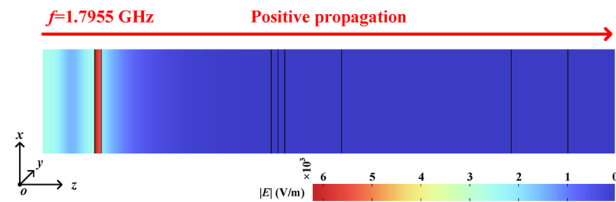


Figure 4. The simulation diagram of electric field energy distribution when EWs propagate positively at 1.7955 GHz.

Considering that the thicknesses of the dielectric layers change due to the perceived alteration or processing errors, **Figure 5** shows the forward and backward transmission spectrum under the presence of both B_1 and B_2 when the values of normalized thickness d are 130, 140, and 150 mm, respectively. When $d = 130 \text{ mm}$, positive and negative TPs are indicated in **Figure 5a**, and their corresponding frequency points are $f = 0.8355 \alpha$ and $f = 0.8372 \alpha$. 210.46 and 176.61 as their Q . In **Figure 5b**, the positive and negative TPs corresponding to $d = 140 \text{ mm}$ severally have 0.8379α , 0.9394α , and 350.69, 295.56 as their frequency points and Q . Under the condition of $d = 150 \text{ mm}$, 0.8399α and 0.8413α are the frequency points of TPs on the positive and negative scales in **Figure 5c**, with Q values of 437.46 and 391.32. It is not difficult to conclude that with the increase of d , the frequency corresponding to TP increases, T decreases, and Q also increases gradually. The main reason is that the increase of d leads to the defect layer being thicker, which enhances the LDMR, produces the blueshift, and makes TP sharper. At the same time, the frequency differences Δf of positive and negative TPs corresponds to $d = 130, 140, \text{ and } 150 \text{ mm}$ are $1.62 \times 10^{-3} \alpha$, $1.5 \times 10^{-3} \alpha$, and

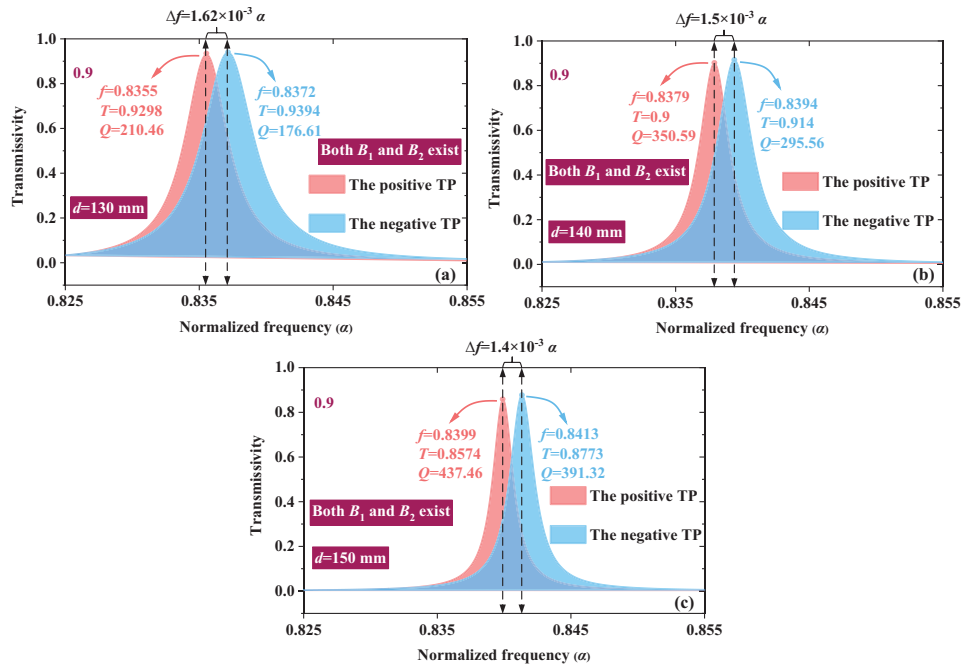


Figure 5. The transmission spectrum of positive and negative TPs under different d when both B_1 and B_2 exist. a) $d = 130$ mm, b) $d = 140$ mm, and c) $d = 150$ mm.

$1.4 \times 10^{-3} \alpha$, respectively. It indicates that with the increase of d , the frequency difference Δf of anteroposterior TP decreases, and the Janus performance of metastructure weakens.

To select the appropriate incident angle to achieve the optimal Janus function, when B_1 and B_2 are both present, **Figure 6** shows the TPs when EWs incident vertically, 10° , 20° , 30° , and 40° in the positive and negative directions, respectively. It can be seen that with the increase of incident angle, the positive and negative TPs generate blueshift. In addition, the frequency difference Δf between TPs corresponding to the forward and backward scales gradually increases, indicating that Janus performance is enhanced step by step. Nevertheless, **Figure 6** shows the T of positive and negative TP under various angles. The positive TP value of incident angle 40° , which embodies the best performance of Janus, is less than 0.9, which dissatisfies the requirements of the T required for AND logic gate and physical quantities detection. In conclusion, considering that the property of Janus can be improved as far as possible under the condition that the TP value is greater than 0.9, 30° is selected as the suitable incident angle of EWs.

To study the ability and logic operation of the JMS to detect the RI, the dielectric A is used as the sensing region in the 1D JMS. The AND logic operation is analyzed. (Supporting Information Part 1 gives the 3D overhead maps of RI detection when EWs propagate from positive and negative directions). Keeping logical operations within the RI detection range can undoubtedly be applied to many more situations, providing quite constructive suggestions for the implementation of logical operation gates with simple structures that are easy to manufacture and analyze. To evaluate the RI detection performance of the JMS, important parameters such as S , Q , the figure of merit (FOM), and

DL are introduced for evaluation. The relevant expressions are as follows^[48]

$$S = \frac{\Delta f}{\Delta x} \quad (12a)$$

$$Q = \frac{f_T}{\text{FWHM}} \quad (12b)$$

$$\text{FOM} = \frac{S}{\text{FWHM}} \quad (12c)$$

$$\text{DL} = \frac{f_T}{20SQ} \quad (12d)$$

where Δx and Δf , respectively, represent the increment of the physical quantities to be measured and the related increment change of TP frequency. The frequency and half-height width of the transmission resonant peak are severally represented by f_T and full width at half maximum (FWHM). An excellent sensor has higher S , Q , FOM, and lower DL, which means that TP can be more easily distinguished.

On the positive scale, when both B_1 and B_2 exist, the linear fitting method is used to select the RI detection points along the horizontal axis with equal spacing of $n_A = 0.15$, and the linear fitting relation (LFR) shown in **Figure 7a** is obtained. In the range of $n_A = \approx 2-2.75$, LFR is $f = -0.096n_A + 1.028$, $S = 0.096 \alpha \text{ RIU}^{-1}$, indicating that sensitive detection can be achieved. The linear regression coefficient of determination R^2 is introduced to assess the degree of the linear fit. The larger the goodness of fit is, the higher the degree of explanation of the independent variable to the dependent variable is, the closer the R^2 value is to 1,

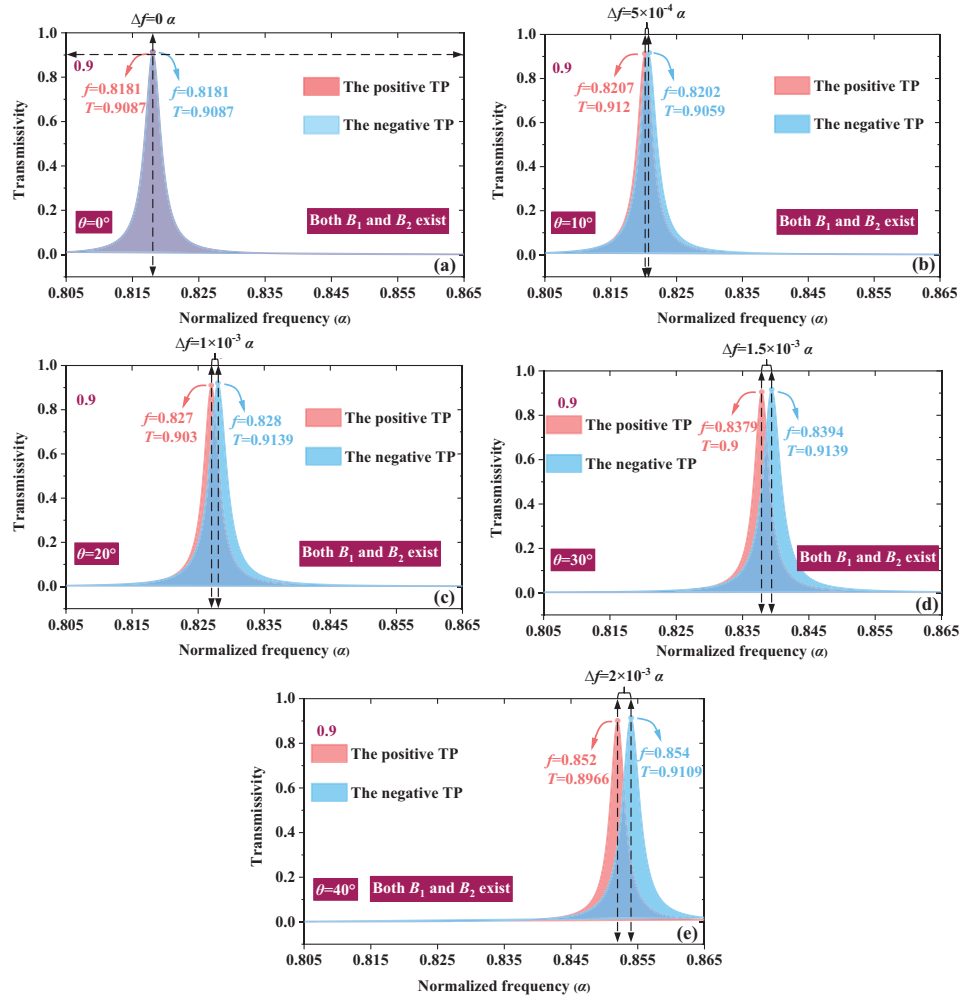


Figure 6. The transmission spectra belong to positive and negative scales under different incident angles. a) $\theta = 0^\circ$, b) $\theta = 10^\circ$, c) $\theta = 20^\circ$, d) $\theta = 30^\circ$, and e) $\theta = 40^\circ$.

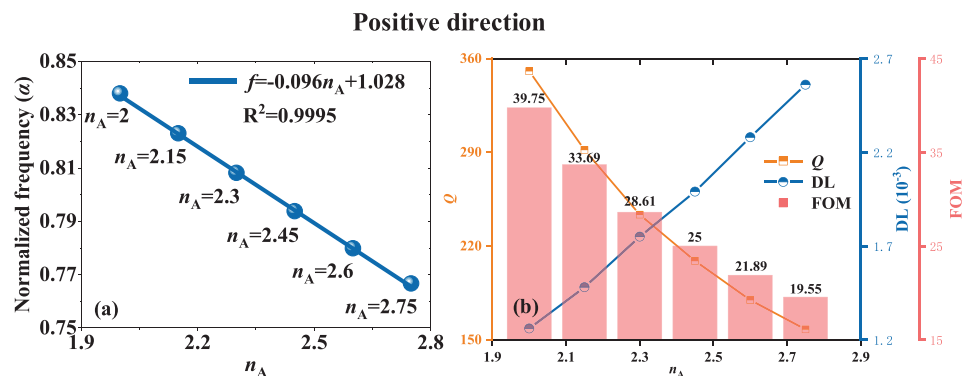


Figure 7. The performance of the positive RI detection. a) The LFR between n_A and normalized frequency, and b) the Q , FOM, and DL under different n_A .

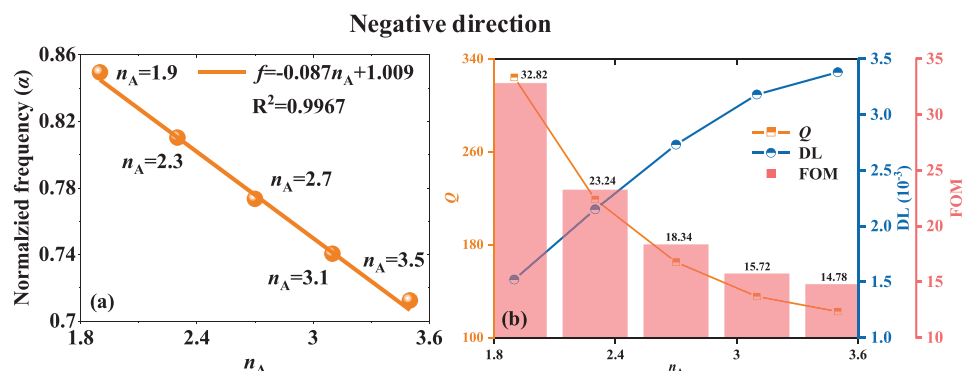


Figure 8. The performance of the negative RI detection. a) The LFR between n_A and normalized frequency, and b) the Q, FOM, and DL under different n_A .

and the more dense the observation points are near the regression line. In Figure 7a, $R^2 = 0.9995$, indicating a considerable linear relationship. When EWs propagate from the negative direction, **Figure 8a** presents the LFR in the RI range of ≈ 1.9 – 3.5 , $f = -0.087n_A + 1.009$. $0.087 \alpha \text{ RIU}^{-1}$ and 0.9967 correspond to S and R^2 , respectively, symbolizing the superiority of LFR. In the following, the performance of the JMS is determined in detail by calculating Q, FOM, and DL within the detection range. For positive detection, the range of parameters can be obtained by finding the maximum and minimum values of parameters within the linear range of ≈ 2 – 2.75 . As exhibited in Figure 7b, the ranges of Q, FOM, and DL are ≈ 157.73 – 350.59 , ≈ 19.55 – 39.75 RIU^{-1} , and 1.26×10^{-3} – $2.56 \times 10^{-3} \text{ RIU}$, respectively. Q decreases with the increase of n_A , as the reason why the correlative TP peak shape gradually becomes blunt. In contrast, on the negative detection scale, the relevant value ranges displayed in Figure 8b are ≈ 122.39 – 324 , ≈ 14.78 – 32.82 RIU^{-1} , and $\approx 1.52 \times 10^{-3}$ – $3.38 \times 10^{-3} \text{ RIU}$. The average can identify with the overall situation. The average values of Q, FOM, and DL on the positive and negative scales are 238.68 , 28.08 RIU^{-1} , $1.89 \times 10^{-3} \text{ RIU}$, and 160.93 , 17.48 RIU^{-1} and $2.16 \times 10^{-3} \text{ RIU}$. As a result, the JMS has good RI detection performance in the forward and backward directions. Additionally, the forward detection has a larger FOM and smaller DL compared to the backward one, which means that the positive scale has a greater S in the same detection range. Furthermore, material A, which is nondispersive, possesses a constant RI in any energy range. When the dielectric A layer is selected as the sensing area, the analyte is identified by RI measurement. A precise technique base on microinfiltration technology by hollow submicrometer-size pipettes can be taken to inject the analyte into the sensing layers.^[49,50] By detecting the frequency of the resonant TP and putting it into the corresponding linear equation, the relevant RI of the analyte can be calculated, and thus the substance can be derived. It is worth emphasizing that for traditional sensors, a single detection method often leads to poor accuracy of physical quantities, which can be improved if there are multiple detection methods, such as the proposed multiscale RI detection. On the positive and negative scales, the proposed JMS has different LFR, S , and DL within the same RI detection range of ≈ 2 – 2.75 , which can realize multiple detection methods for the same substance to improve the accuracy. For instance, the creatinine concentration is an important index for evaluating renal

Table 3. Creatinine concentration ($\mu\text{mol L}^{-1}$) with attributed RI.

Creatinine concentration [$\mu\text{mol L}^{-1}$]	RI
80.9	2.661
81.43	2.655
82.3	2.639
83.3	2.610
84.07	2.589
85.28	2.565

function. **Table 3** shows the relationship between the creatinine concentration ($\mu\text{mol L}^{-1}$) and RI.^[51] An unknown concentration of creatinine solution is injected into the dielectric layer A with a precise technique based on microinfiltration technology by hollow submicron size pipettes,^[52] assuming that the resonant TP frequency measured positively is 0.7747α , the RI of the analyte can be calculated as 2.639 according to the LFR. To improve the detection accuracy, the measurement is carried out on a negative scale. If the TP frequency measured is 0.7794α , the RI is verified to be the exact value of 2.639, and the analyte can be known as the creatinine solution with a concentration of $82.3 \mu\text{mol L}^{-1}$.

The proposed JMS can detect the magnetic induction intensity. The following content discusses the measurement of magnetic field strength B_1 . (Supporting information Part 2 shows the 3D overhead maps of B_1 detection). As indicated in **Figure 9a,c**, $f = -9.42 \times 10^{-3} B_1 + 0.857$ and $f = -4.47 \times 10^{-3} B_1 + 0.848$ are the positive and negative correspondence LFR in the B_1 range of forward ≈ 2 – 2.15 T and backward ≈ 1.96 – 2.16 T under the AND logic gate “1 AND 1 = 1.” Among them, 9.42×10^{-3} and $4.47 \times 10^{-3} \alpha \text{ T}^{-1}$ are the S , which is considerable. In addition, the values of R^2 are 0.9999 and 0.9998, manifesting that LFR is very reliable. In the measurement range of ≈ 1.55 – 1.65 T , Figure 9b indicates that the mean values of Q, FOM, and DL are 324.81 , 3.66 T^{-1} , and $1.37 \times 10^{-2} \text{ T}$. 280.87 , 1.5 T^{-1} and $3.37 \times 10^{-2} \text{ T}$ correspond to the average values of Q, FOM, and DL in the B_1 range of ≈ 1.96 – 2.16 T are shown in Figure 9d, which can meet the requirements of sensors performance. In addition, under the condition that only the applied MFS B is considered to affect the plasma-producing magneto-optical effect, the plasma layer is the sensitive region, so the JMS with these promising performance parameters can

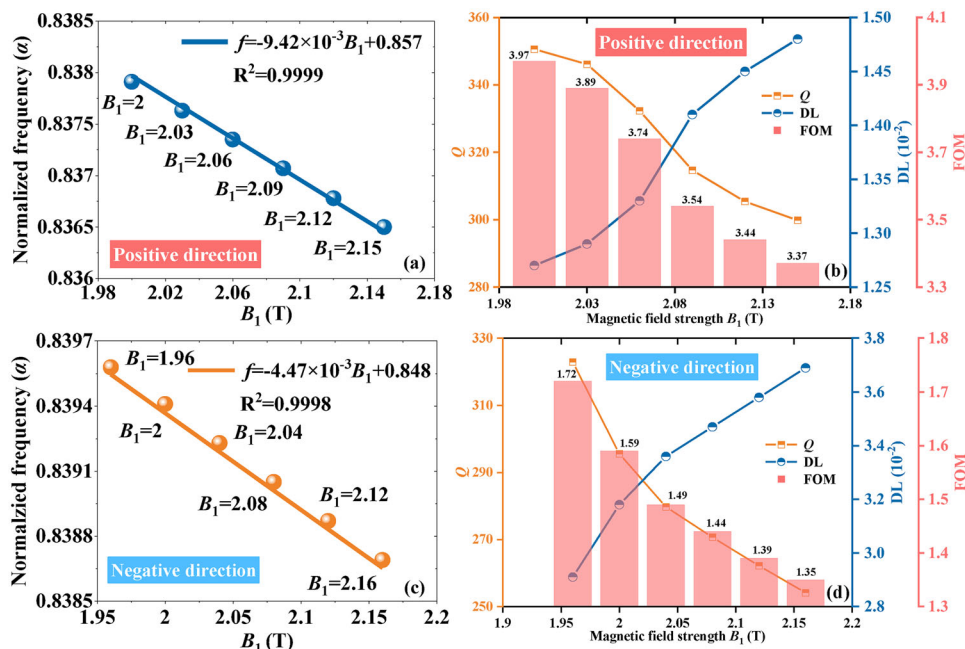


Figure 9. The performance of the B_1 detection. On the positive scale: a) The LFR between B_1 and normalized frequency. b) The Q, FOM, and DL under different B_1 . On the negative scale: c) The LFR between B_1 and normalized frequency. d) The Q, FOM, and DL under different B_1 .

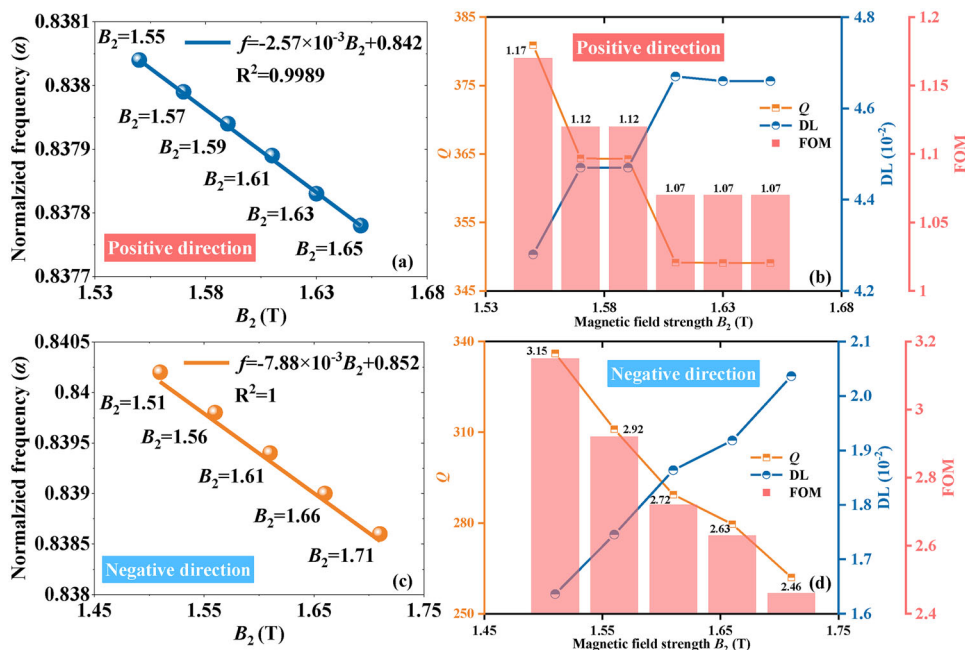


Figure 10. The performance of the B_2 detection. On the positive scale: a) The LFR between B_2 and normalized frequency, and b) The Q, FOM, and DL under different B_2 . On the negative scale: c) The LFR between B_2 and normalized frequency, and d) The Q, FOM, and DL under different B_2 .

be used to accurately measure the drift of TPs at two scales, and then evaluate the value of magnetic induction intensity.

When B_1 exists or does not exist, the TP simulation diagram can be obtained through the change of B_2 , which intuitively illustrates the relationship between the normalized frequency of the target resonance peak and B_2 (Supporting Information Part 2 indicates the 3D overhead maps of B_2 detection). When

both B_1 and B_2 exist, using the linear fitting method, in the B_2 range of forward ≈ 1.55 – 1.65 T and backward ≈ 1.51 – 1.71 T, the LFR belonging to positive and negative B_2 detection is displayed in **Figure 10a,c**. LFR is $f = -2.57 \times 10^{-3} B_2 + 0.842$ and $f = -7.88 \times 10^{-3} B_2 + 0.852$, and S is $-2.57 \times 10^{-3} \alpha T^{-1}$ and $-7.88 \times 10^{-3} \alpha T^{-1}$, respectively. 0.9989 and 1 are the relevant R^2 , which is excellent. **Figure 10b,d** exhibits the Q, FOM, and DL values of

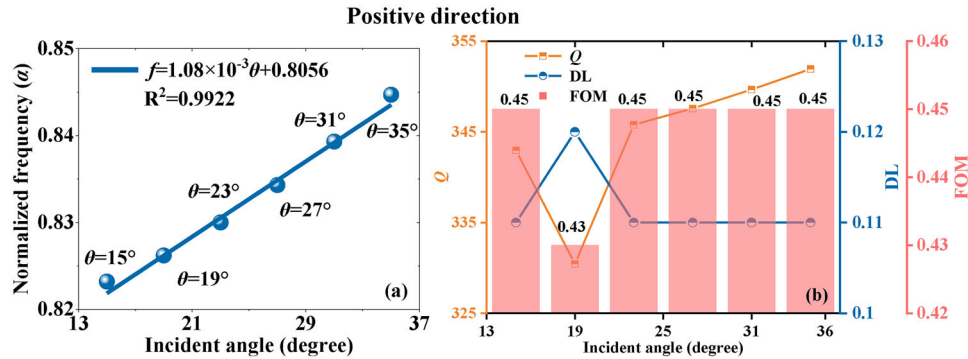


Figure 11. The performance of the positive angle detection. a) The LFR between incident angle and normalized frequency, and b) The Q, FOM, and DL under different incident angles.

each correspondence B_2 detection point. With the increase of B_2 , Q, and FOM gradually decreased and severally reached the minimum values of 349.08, 1.07 T^{-1} , and 262.03, 2.46 T^{-1} when forward $B_2 = 1.65$ T and backward $B_2 = 1.71$ T, which are still sufficient values for detection. The average values of positive and negative DL are 4.54×10^{-2} and 1.82×10^{-2} T, respectively. MFS detection with different precision can be achieved within the same detection range.^[53,54]

The measurement of the rotation angle of the bridge support is an important standard to evaluate the state of the bridge. The existing tiltmeter does not have sufficient resolution and precision to measure the weak angle change.^[55] The spacecraft docking and pose adjustment have very harsh requirements on the angle.^[56] A system utilizing cameras and image processing techniques has been developed to measure weak angle change.^[57] However, this system is expensive and needs to carry very complex equipment. Therefore, the high-precision angle detection realized by the proposed JMS with compact structure, small size, and low manufacturing cost is urgently needed, which is convenient to carry and apply to multiple scenarios. Moreover, because the GHz band is used which owns a long transmission wavelength, the sensor can easily avoid the obstacles in the way of EWs propagation, so it is less affected by the application environment. The performance of high-precision angle detection is discussed below. The change in the incident angle has a significant effect on the transmission wavelength shift according to the Bragg–Snell law^[58–60]

$$m\lambda = 2d_w \sqrt{n_{\text{eff}}^2 - \sin^2 \theta} \quad (13)$$

where m is the order of diffraction, d_w is the thickness of the whole metastructure, λ is the wavelength of the stopband, n_{eff} is the effective refractive index of the whole metastructure, θ is the incident angle. Therefore, when TP is generated, along with the angle of EWs incident into the JMS varying, the TP frequency is found to change accordingly, and high-precision angle sensing with the accuracy of 0.01° is realized based on this (Supporting Information Part 3 gives the simulated diagrams to prove that the accuracy of the angle sensor is 0.01°). We combined the metastructure with θ -2 θ motorized rotation stage (Sigma Koki) and a two-axis stepping motor drive controller with 0.01° at each step to form a test system, which can adjust the incidence angle.^[61] The sensitive area is the surface of the first layer composed of di-

electric C. When EWs are incident from the front, the four cases correspond to the presence or absence of the two input levels following the AND logic gate (Supporting Information Part 4 exhibits the 3D overhead maps of the angle detection when EWs propagate positively). Under the condition that both B_1 and B_2 exist, the discussion of the sensing performance is presented in **Figure 11**. The incident angle detection points are selected with equal spacing of 4° . After linear fitting, the LFR of angle detection in the range of $\approx 15^\circ$ – 35° is displayed in **Figure 11a**, $f = 1.08 \times 10^{-3} \theta + 0.8056$, $S = 1.08 \times 10^{-3} \alpha$ degree $^{-1}$. When d is 140 mm, the value of S is approximately equal to 1.45×10^7 degree $^{-1}$, which is ultrahigh. Hence, high-precision angle detection can be carried out on the surface of the first dielectric layer. $R^2 = 0.9922$ represents the reliability of LFR. **Figure 11b** shows the Q, FOM, and DL belonging to each detection point. The average values of Q, FOM, and DL are 344.73, 0.447 degree $^{-1}$, and 0.111 degrees, respectively, which meet the performance requirements of angle sensing.

Due to the phenomenon that propagation frequency varies on the negative scale caused by the adjustment of the incident angle between 22° and 52° under the presence of both B_1 and B_2 , the LFR belonging to the 3D overhead maps of negative angle detection is indicated in **Figure 12a**. (The 3D overhead maps of negative angle detection are gained from Part 4 in the Supporting Information). In the range of θ from 22° to 52° , $f = 1.48 \times 10^{-3} \theta + 0.7956$, $S = 1.48 \times 10^{-3} \alpha$ degree $^{-1}$, and when $d = 140$ mm, 1.99×10^7 degree $^{-1}$ is the corresponding S , which proves that high-precision angle detection can be achieved. Measurement points are concentrated near the regression line as demonstrated by $R^2 = 0.9965$. **Figure 12b** exhibits the TP assessment for each measurement point. The values of Q and FOM increased continuously, indicating that the peak deformation of TP is sharper and the detection precision increased as the θ moved in a bigger direction. The average values of Q, FOM, and DL are 311.9, 0.54 degree $^{-1}$, and 9.24×10^{-2} degree, respectively, which can realize the function of angle sensing.

Plasma processing plays a key role in the advancement of modern semiconductor manufacturing processes, especially in etching and deposition applications.^[62] For these plasmon-based material processes, the plasma density is one of the most important parameters to determine the plasma properties, which in turn controls the processing results. Therefore, the development of sensors for detecting plasma density has attracted a great deal

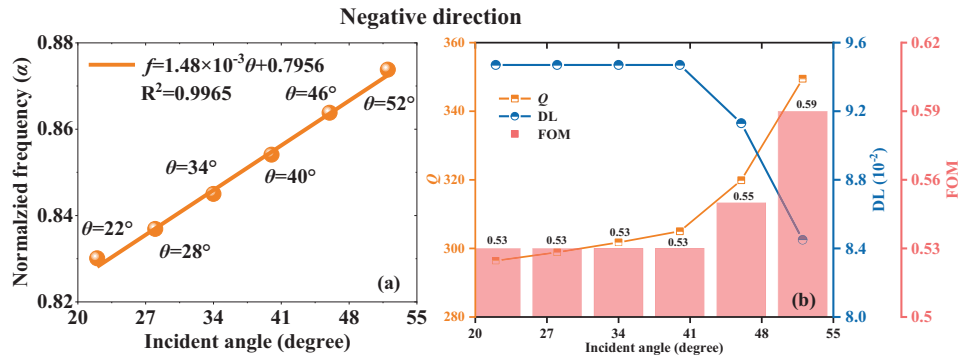


Figure 12. The performance of the negative angle detection. a) The LFR between incident angle and normalized frequency, and b) The Q, FOM, and DL under different incident angles.

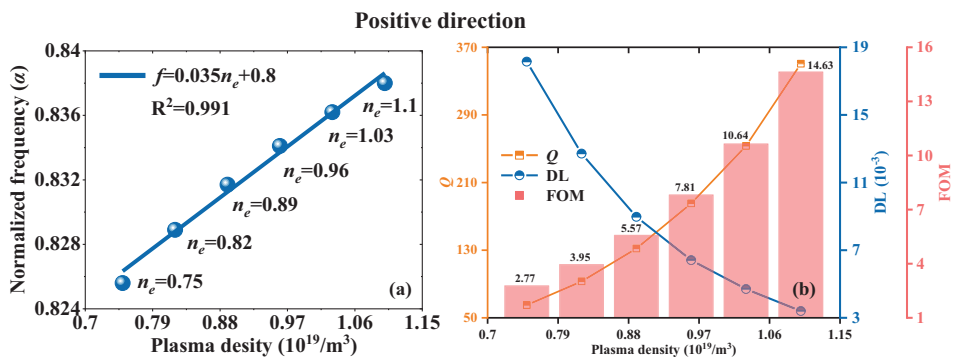


Figure 13. The performance of the positive n_e detection. a) The LFR between n_e and normalized frequency, and b) The Q, FOM, and DL under different n_e .

of attention.^[63–65] The plasma layers in the metastructure are controllable alternating-current discharge sealed containers, and the variable discharge current controls the plasma density.^[66] By setting the plasma layer as the sensitive part, the JMS can be utilized for plasma density detection. It should be emphasized that in the JMS, although the magnetic field intensities applied to plasma₁ and plasma₂ layers are different, plasma₁ and plasma₂ are strictly allowed to have the same plasma density, which is convenient to change the overall one. **Figures 13a** and **14a** show the LFR of positive and negative plasma density detection when satisfies the AND logic gate “1 AND 1 = 1,” $f = 0.035 n_e + 0.8$ and

$f = 0.034 n_e + 0.8022$ corresponding to the n_e range of forward $\approx 0.75\text{--}1.1 \times 10^{19} \text{ m}^{-3}$ and backward $\approx 0.58\text{--}1.13 \times 10^{19} \text{ m}^{-3}$. Where $0.035 \text{ am}^3/10^{19}$ and $0.034 \text{ am}^3/10^{19}$ are the correlative S, respectively. The values of R^2 are 0.991 and 0.9921 indicating the high reliability of the LFR. Detailed Q, FOM, and DL are presented in **Figures 13b** and **14b**. It can be seen that the numerical curve of Q gradually rises with the increase of n_e , which is consistent with the change of peak shape of TP in 3D overhead maps of n_e under the presence of both B_1 and B_2 (Supporting Information Part 5 gives the 3D overhead maps of n_e detection on the positive and negative scales). The average values of positive and negative

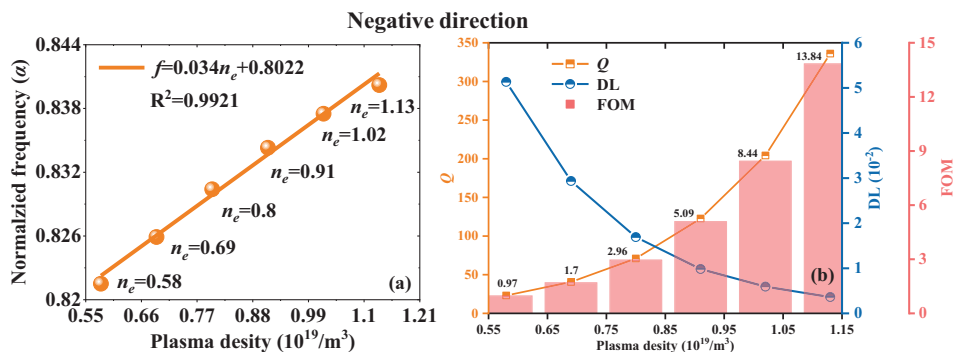


Figure 14. The performance of the negative n_e detection. a) The LFR between n_e and normalized frequency, and b) The Q, FOM, and DL under different n_e .

Table 4. The performance of the published reports compared with such a JMS.

Refs.	Janus	Multifunction	Physical quantities detection			Logic gate
[67]	No	No			None	AND
[68]	No	No			None	AND
[69]	No	No	MFS		Range $\approx 30\text{--}90$ Oe S 0.817 nm Oe $^{-1}$	None
[70]	No	No	RI		Range $\approx 1.362\text{--}1.366$ S 303 376 nm RIU $^{-1}$	None
[71]	Yes	No	RI	Positive	Range $\approx 1.35\text{--}2.09$ S 132 MHz RIU $^{-1}$	None
				Negative	Range $\approx 1\text{--}1.57$ S 40.7 MHz RIU $^{-1}$	
[72]	No	Yes	RI		Range $\approx 1.455\text{--}1.469$ S 56.815 dBm RIU $^{-1}$	None
				Temperature	Range $\approx 22\text{--}42$ °C S 0.0281 dBm °C $^{-1}$	
This work	Yes	Yes	RI	Positive	Range $\approx 2\text{--}2.75$ S 0.095α RIU $^{-1}$	AND
				Negative	Range $\approx 1.9\text{--}3.5$ S 0.086α RIU $^{-1}$	
			MFS		Indicated in the article	
			Angle		Indicated in the article	
			n_e		Indicated in the article	

scales sensing performance parameters Q, FOM, and DL are 179.9, 7.56×10^{-19} , $9.06 \times 10^{-3} \times 10^{19} \text{ m}^{-3}$, and 132.95, 5.5×10^{-19} , $19.49 \times 10^{-2} \times 10^{19} \text{ m}^{-3}$, respectively, which proves the feasibility of n_e sensing.

The means of simulation, the transmission spectrum, the 3D overhead maps of TP, and the calculation of S, R^2 , Q, FOM, DL and are simulated by MATLAB 2020. The electric field distribution diagram is simulated by the finite-difference time-domain (FDTD) method. The method of searching for optimization is used to gradually obtain more appropriate values by constantly adjusting parameters (such as thickness and refractive index of dielectric layers).

Finally, to provide a systematic and intuitive description of this novel JMS, previously reported devices of related designs with outstanding performance are summarized, which are listed in **Table 4** for comparison. In terms of multifunction, Janus property, and physical quantities detection performance, it is concluded that the 1D JMS which is proposed in this paper is advanced and valuable, and is generally superior to those mentioned in the past.

3. Conclusions

In summary, the multifunction and physical detection performance of the proposed 1D JMS based on magnetized plasma material are theoretically investigated under TM polarization. The Janus property is achieved through the asymmetric arrangement of the different dielectric layers and the anisotropy of the plasma,

which equips the MS with a multiscale feature. The introduction of the plasma layer not only gives the structure a magnetic tuning function but also acts as a defect layer to excite the LDMR, resulting in a sharp TP. The AND logic gate can be formed on the positive and negative scales by discriminating the TP values. By locking the TP normalized frequency, the RI, magnetic field, angle, and plasma density can be detected in the GHz band by changing the relevant physical quantities in different sensitive regions. On the positive and negative scales, the measurement ranges of RI correspond to $\approx 2\text{--}2.75$ and $\approx 1.9\text{--}3.5$, the ranges of magnetic field strength B_1 are $\approx 2\text{--}2.15$ and $\approx 1.96\text{--}2.16$ T, the ranges of MFS B_2 are $\approx 1.55\text{--}1.65$ and $\approx 1.51\text{--}1.71$ T, the ranges of angle are $\approx 15^\circ\text{--}35^\circ$ and $\approx 22^\circ\text{--}52^\circ$, the measuring ranges of the plasma density are $\approx 0.75\text{--}1.1$ (10^{19} m^{-3}) and $\approx 0.58\text{--}1.13$ (10^{19} m^{-3}), respectively. The positive and negative scales possess different measurement ranges of physical quantities, and the corresponding S, Q, FOM, and DL are intuitive representations of the Janus property belonging to the MS. This new multifunctional and multiscale JMS has a broad prospect for logic devices, optical signal processors, sensors, and is suitable for multiple application scenarios, which provides a new way for the design of novel multifunctional devices.

Supporting Information

Supporting Information is available from the Wiley Online Library or from the author.

Acknowledgements

This work was supported by the National College Student Innovation Training Program (Grant No. 202210293014Z).

Conflict of Interest

The authors declare no conflict of interest.

Data Availability Statement

The data that support the findings of this study are available on request from the corresponding author. The data are not publicly available due to privacy or ethical restrictions.

Keywords

Janus metastructure, logic gate, metastructures, multifunctional devices

Received: October 22, 2022

Revised: December 21, 2022

Published online:

-
- [1] Y. Zhu, L. Cao, A. Merkel, *Nat. Commun.* **2021**, *12*, 7089.
- [2] P. Gennes, *Phys. Polym. Surf. Interfaces* **1992**, *1992*, 55.
- [3] C. Casagrande, *CR Acad. Sci. Ser. II* **1998**, *306*, 1423.
- [4] A. Walther, A. H. E. Müller, *Soft Matter* **2008**, *4*, 663.
- [5] S. H. Hu, X. Gao, *J. Am. Chem. Soc.* **2010**, *132*, 7234.
- [6] L. Y. Wu, B. M. Ross, S. G. Hong, *Small* **2010**, *6*, 503.
- [7] J. Jiang, H. Gu, H. Shao, *Adv. Mater.* **2008**, *20*, 4403.
- [8] C. Huck, J. Vogt, M. Sendner, *ACS Photonics* **2015**, *2*, 1489.
- [9] K. Chen, G. Ding, G. Hu, *Adv. Mater.* **2020**, *32*, 1906352.
- [10] P. Yu, J. Li, S. Zhang, *Nano Lett.* **2018**, *18*, 4584.
- [11] M. Yin, X. Yong Tian, H. Xue Han, *Appl. Phys. Lett.* **2012**, *100*, 124101.
- [12] H. Xu, S. Bie, Y. Xu, *Composites, Part A* **2016**, *80*, 111.
- [13] L. Yin, J. Doyhamboure, X. Tian, *Composites, Part B* **2018**, *132*, 178.
- [14] Z. Yang, F. Luo, W. Zhou, *J. Alloys Compd.* **2017**, *699*, 534.
- [15] Q. Liang, Z. Yang, J. Guo, *J. Mater. Sci.: Mater. Electron.* **2020**, *31*, 19242.
- [16] D. Schurig, J. J. Mock, B. J. Justice, *Science* **2006**, *314*, 977.
- [17] Z. Jiang, Q. Liang, Z. Li, *Adv. Opt. Mater.* **2019**, *7*, 1900475.
- [18] N. Landy, D. R. Smith, *Nat. Mater.* **2013**, *12*, 25.
- [19] L. Liu, X. Zhang, M. Kenney, *Adv. Mater.* **2014**, *26*, 5031.
- [20] L. Zhang, S. Mei, K. Huang, *Adv. Opt. Mater.* **2016**, *4*, 818.
- [21] L. Cong, N. Xu, J. Han, *Adv. Mater.* **2015**, *27*, 6630.
- [22] J. K. Gansel, M. Thiel, M. S. Rill, *Science* **2009**, *325*, 1513.
- [23] M. L. N. Chen, L. J. Jiang, W. E. I. Sha, *J. Appl. Phys.* **2016**, *119*, 064506.
- [24] V. Dhasarathan, S. K. Sahu, T. K. Nguyen, *Optik* **2020**, *202*, 163723.
- [25] S. R. Entezar, M. K. Habil, *J. Magn. Magn. Mater.* **2018**, *449*, 33119.
- [26] P. Wu, J. Zhang, Y. Xuan, P. Wu, *Appl. Laser* **2016**, *36*, 735.
- [27] V. Jandieri, T. Onoprishvili, R. Khomeriki, *Opt. Quantum Electron.* **2019**, *51*, 121.
- [28] Z. Zhao, Y. Wang, C. Guan, *Photonix* **2022**, *3*, 15.
- [29] L. P. Caballero, M. L. Povinelli, J. C. Ramirez, *Opt. Express* **2022**, *30*, 1976.
- [30] Z. Zhao, Y. Wang, X. Ding, H. Li, J. Fu, K. Zhang, S. N. Burokur, Q. Wu, *Photon. Res.* **2022**, *10*, 316.
- [31] Z. Wang, G. Hu, X. Wang, *Nat. Commun.* **2022**, *13*, 2188.
- [32] X. Ding, Z. Wang, G. Hu, *Photonix* **2020**, *1*, 16.
- [33] H. Abdeldayem, D. O. Frazier, *Commun. ACM* **2007**, *50*, 60.
- [34] L. Dai, Y. Zhang, H. Zhang, *Appl. Phys. Express* **2019**, *12*, 075003.
- [35] J. Sui, D. Zhang, H. Zhang, *J. Phys. D: Appl. Phys.* **2022**, *55*, 415001.
- [36] P. Bing, J. Sui, G. Wu, *Plasmonics* **2020**, *15*, 1071.
- [37] Y. Zhao, Y. Zhang, R. Lv, *J. Lightwave Technol.* **2017**, *35*, 3440.
- [38] Y. Yang, F. Yang, H. Wang, *J. Lightwave Technol.* **2015**, *33*, 2566.
- [39] M. Sovizi, M. Aliannezhadi, *J. Opt. Soc. Am. B* **2019**, *35*, 3450.
- [40] Y. Liu, S. Li, H. Chen, *J. Phys. D: Appl. Phys.* **2020**, *53*, 115107.
- [41] S. Guo, C. Hu, H. Zhang, *J. Opt.* **2020**, *22*, 105101.
- [42] L. Lewin, *Proc. Inst. Electr. Eng., Part III: Radio Commun. Eng.* **1947**, *94*, 65.
- [43] X. Liu, Q. Zhao, C. Lan, *Appl. Phys. Lett.* **2013**, *103*, 031910.
- [44] L. Xuan, X. Kong, J. Wu, *Appl. Magn. Reson.* **2021**, *52*, 649.
- [45] F. Fan, S. J. Chang, W. H. Gu, *IEEE Photonics Technol. Lett.* **2012**, *24*, 2080.
- [46] L. Qi, Z. Yang, F. Lan, *Phys. Plasmas* **2010**, *17*, 042501.
- [47] A. H. Aly, D. Mohamed, M. A. Mohaseb, *Int. J. Mod. Phys. B* **2019**, *33*, 1950397.
- [48] Z. A. Zaky, A. M. Ahmed, A. S. Shalaby, *Sci. Rep.* **2020**, *10*, 9736.
- [49] F. Intonti, S. Vignolini, V. Türck, Rewritable photonic circuits, *Appl. Phys. Lett.* **2006**, *89*, 211117.
- [50] S. Arafa, M. Bouchemat, T. Bouchemat, *Opt. Commun.* **2017**, *384*, 93.
- [51] A. H. Aly, D. Mohamed, M. A. Mohaseb, *RSC Adv.* **2020**, *10*, 31765.
- [52] F. Intonti, S. Vignolini, V. Türck, *Appl. Phys. Lett.* **2006**, *89*, 211117.
- [53] S. Santi, V. Musi, E. Descrovi, *ChemPhysChem* **2013**, *14*, 3476.
- [54] Y. N. Zhang, A. Zhang, B. Han, *J. Opt.* **2018**, *20*, 065401.
- [55] Y. S. Park, J. A. Agbayani, J. H. Lee, *J. Sens.* **2016**, *12*, 192393.
- [56] L. Yuan, F. Yunfeng, S. Yin hao, *Bingqi Zhuangbei Gongcheng Xuebao* **2018**, *39*, 8.
- [57] H. Jeon, Y. Bang, H. Myung, *Smart Mater. Struct.* **2011**, *20*, 045019.
- [58] A. H. Aly, Z. A. Zaky, *Cryogenics* **2019**, *104*, 102991.
- [59] R. C. Schroden, M. Al-Daous, C. F. Blanford, *Chem. Mater.* **2002**, *14*, 3305.
- [60] A. H. Aly, M. Ismaeel, E. Abdel-Rahman, *Opt. Photonics J.* **2012**, *2*, 2.
- [61] H. R. Gwon, S. H. Lee, *Mater. Trans.* **2010**, *51*, 1150.
- [62] Y. Liang, K. Kato, K. Nakamura, *Jpn. J. Appl. Phys.* **2011**, *50*, 116101.
- [63] C. Scharwitz, M. Böke, S. H. Hong, *Plasma Processes Polym.* **2007**, *4*, 605.
- [64] K. H. You, S. J. You, D. W. Kim, *Thin Solid Films* **2013**, *547*, 250.
- [65] G. S. Gogna, C. Gaman, S. K. Karkari, *Appl. Phys. Lett.* **2012**, *101*, 042105.
- [66] B. Wang, M. A. Cappelli, *Appl. Phys. Lett.* **2016**, *108*, 161101.
- [67] A. Mohebzadeh-Bahabady, S. Olyaei, *Optoelect. Lett.* **2020**, *16*, 477.
- [68] M. M. Gupta, S. Medhekar, *Optik* **2016**, *127*, 1221.
- [69] D. Ge, H. Chen, Z. Hu, *J. Magn. Magn. Mater.* **2022**, *545*, 168753.
- [70] Y. Zhang, L. Wang, P. Jia, *Optik* **2022**, *256*, 168488.
- [71] Y. T. Xiang, B. F. Wan, H. F. Zhang, *IEEE Sens. J.* **2021**, *21*, 19984.
- [72] S. M. K. Alawsy, M. A. Jabbar, *Opt. Photonics J.* **2018**, *8*, 83004.